Journal of Alloys and Compounds 834 (2020) 154992

Contents lists available at ScienceDirect

Journal of Alloys and Compounds

journal homepage: http://www.elsevier.com/locate/jalcom

3D core-shell WO_3@α-Fe_2O_3 photoanode modified by ultrathin FeOOH layer for enhanced photoelectrochemical performances

Jin Zhang [a, *], Gangqiang Zhu [b, **], Weiguo Liu [a], Yingxue Xi [a], D.A. Golosov [c], S.M. Zavadski [c], S.N. Melnikov [c]

[a] Shaanxi Province Key Laboratory of Thin Films Technology and Optical Test, School of Optoelectronic Engineering, Xi'an Technological University, Xi'an, 710032, PR China
[b] School of Physics and Information Technology, Shaanxi Normal University, Xi'an, 710062, PR China
[c] Belarusian State University of Informatics and Radioelectronics, 6 P. Brovka str., 220013, Minsk, Belarus

ARTICLE INFO

Article history:
Received 11 March 2020
Received in revised form
27 March 2020
Accepted 28 March 2020
Available online 5 April 2020

Keywords:
WO_3
α-Fe_2O_3
Photoanode
FeOOH layer
Photoelectrochemical water splitting

ABSTRACT

The solar light absorption efficiency as well as the carrier separation and transfer efficiency in the bulk and on the surface of the photoanodes are still the main challenges for efficient photoelectrochemical (PEC) water splitting. Hence, in this work, a 3D core-shell WO_3@α-Fe_2O_3 photoanode modified by ultrathin FeOOH layer was designed and fabricated for the first time to maximize respective merits of 1D WO_3 (excellent electron transport pathways), α-Fe_2O_3 (strong visible light absorption) and FeOOH (a hole transfer) to achieve efficient PEC performances. As a result, the as-fabricated WO_3@α-Fe_2O_3/FeOOH photoanode exhibits a 120 mV negatively shift in onset potential and yields a photocurrent density of 1.12 mA/cm^2 at 1.23 V vs. RHE, which is 1.72 and 3.73 times than that of WO_3@α-Fe_2O_3 and WO_3 photoanodes, respectively. Moreover, this work may provide an effective strategy of maximizing the advantages of each component in the composite photoelectrode to achieve effective PEC performance.

1. Introduction

Since the pioneering work of photoelectrochemical (PEC) water splitting using TiO_2 as the photoanode under solar irradiation was reported by Honda and Fujishima in 1972 [1], the PEC system based on nano-semiconductors working as the workhorse to convert solar energy into hydrogen has acquired interest because it is of great significance to solve environmental crisis and realize sustainable development [2,3]. Consequently, a large number of nano-semiconductor materials have been explored as photoelectrodes for PEC water splitting, especially for the metal oxides (ZnO [4], WO_3 [5,6], α-Fe_2O_3 [7,8], etc) which have been extensively studied because of their earth abundance, low cost and low toxicity [9].

Among them, WO_3 with a band gap of 2.5–2.8 eV possesses a moderate hole diffusion length (~150 nm), excellent electron mobility (12 cm^2 V^{-1} s^{-1}) and the positive valence band edge (3.0 V vs. NHE) for water oxidation, making it emerge as a promising candidate for PEC water splitting [10–12]. However, hindered by its visible light absorption and high carrier recombination efficiency, PEC performances of the single WO_3 photoanodes are still far below that expected. Therefore, coupling WO_3 with the narrow energy band gap semiconductors to construct heterojunction is deemed as an effective way to address the above issues [13]. For example, Liu el al [14] prepared a high quality $BiVO_4$/WO_3 photoanode using an in situ transformation approach, which showed the excellent visible light response and a good photostability. The photocurrent density was up to 2.92 mA/cm^2 at 1.81 V vs. RHE owing to the $BiVO_4$/WO_3 heterojunction structure which is beneficial for charge separation as well as the extended photoresponse range. Similarly, the widely concerned single α-Fe_2O_3 photoanode still suffers from rapidly electron-hole recombination, leading to low PEC performances [15]. Fortunately, α-Fe_2O_3 has a narrow bandgap (E_g = 2.1 eV), which makes it have a strong absorption of visible light, that is, 40% of solar energy can be utilize theoretically [16,17]. Hence, it is necessary to couple WO_3 and α-Fe_2O_3 to form heterojunction structure to exert respective advantages to improve the PEC performances.

In addition, depositing effective water oxidation catalysts including noble metal oxides (IrO_x and RuO_x) and metal-based

* Corresponding author.
** Corresponding author.
E-mail addresses: j.zhang@xatu.edu.cn (J. Zhang), zgq2006@snnu.edu.cn (G. Zhu).

https://doi.org/10.1016/j.jallcom.2020.154992
0925-8388/

materials (Fe, Co, Ni, Mn and Cu) to improve the sluggish oxygen evolution kinetics, resulting in significantly increased PEC performances [18,19]. Particularly, iron oxyhydroxide (FeOOH) has acquired interest due to its earth-abundant, chemically stable, environmentally friendly and higher oxygen evolution reaction activity [20,21]. For instance, Zhang el al [22]. grew the highly crystalline ultrathin β-FeOOH cocatalyst with abundant oxygen vacancies onto $BiVO_4$ photoanode via a facile solution impregnation, and the resulting $BiVO_4$/FeOOH photoanodes exhibited a remarkable photocurrent density of 4.3 mA/cm^{-2} at 1.23 V vs. RHE. Kuang and his colleagues deposited FeOOH on the surface of Fe_2TiO_5 treated with Al^{3+} (Al—Fe_2TiO_5) to improve the PEC performances of Fe_2TiO_5 photoanode [23]. As a result, the Al—Fe_2TiO_5/FeOOH showed a photocurrent density of 0.52 mA/cm^{-2} at 1.23 V vs. RHE, which is about 2.8 and 1.6 times than that of Fe_2TiO_5 and Al—Fe_2TiO_5, respectively, which can be attributed that the surface Al^{3+} treatment accelerates charge transport and the FeOOH layer improves catalytic activity.

Motivated by the above concerns, the α-Fe_2O_3 nanorices were deposited on the surface of one-dimensional (1D) WO_3 nanorods through a hydrothermal method and annealing treatment, followed by depositing FeOOH layer via a facile chemical bath deposition (CBD) method. The novel 3D WO_3@α-Fe_2O_3/FeOOH photoanodes can make greater use the individual merits of 1D WO_3 (excellent electron transport pathways), α-Fe_2O_3 (strong visible light absorption) and FeOOH (a hole transfer) to achieve efficient PEC performances. Moreover, the 3D WO_3@α-Fe_2O_3 heterojunction structure can decrease carrier recombination efficiency and increase carrier separation efficiency. Furthermore, this work is helpful for the design of efficiency photoelectrodes which can improve the efficiency of carrier separation and transfer in the bulk and on the surface as well as extend the response range to achieve enhanced PEC performances.

2. Experimental section

2.1. Synthesis of WO_3 films

The WO_3 films were fabricated on the FTO substrates by hydrothermal method and annealing treatment [24]. In brief, the mixture aqueous solution containing $Na_2WO_4 \cdot 2H_2O$ (2.0 mmol), $K_2C_2O_4 \cdot H_2O$ (0.9 mmol) and HCl (2 mL) was transferred into a Teflon-lined stainless steel autoclave (25 mL) and heated at 180 °C for 12 h. After cooling down to room temperature naturally, the samples were washed with deionized water and then annealed at 550 °C for 2 h.

2.2. Synthesis of WO_3@α-Fe_2O_3 films

The WO_3@α-Fe_2O_3 films were synthesized through a hydrothermal method and annealing treatment. The precursor solution was prepared by mixing $FeCl_3 \cdot 6H_2O$ (0.15 M) and $NaNO_3$ (1 M) in deionized water and using magnetic stirring at room temperature. Then the mixture was transferred into the Teflon-lined stainless steel autoclave heated at 100 °C for 4 h, in which a piece of above obtained sample was leaned against the inner wall. Afterwards, the obtained sample was rinsed with deionized water and then annealed at 550 °C for 2 h to convert FeOOH to α-Fe_2O_3.

2.3. Synthesis of WO_3@α-Fe_2O_3/FeOOH films

The WO_3@α-Fe_2O_3/FeOOH films were fabricated by a facile chemical bath deposition (CBD) method. The as-obtained WO_3@α-Fe_2O_3 film was immersed in a hot aqueous solution (100 °C) of $FeCl_3 \cdot 6H_2O$ (0.15 M) and $NaNO_3$ (1 M) for 5 min. Then, the samples were gently rinsed with deionized water and dried at 60 °C for 10 h. The schematic preparation process of the WO_3@α-Fe_2O_3/FeOOH composite structure is illustrated in Fig. 1.

2.4. Characterization

X-ray diffraction (XRD) patterns were recorded by an X-ray diffractometer (D/Max-2500, Rigaku) with Cu Kα radiation. Scanning electron microscopy (SEM) images were collected with a field-emission scanning electron microscope (JEOL JSM-7400F) attached with the energy dispersive spectrum (EDS). Transmission electron microscopy (TEM) were performed on a transmission electron microscope (JEOL JEM-2100). X-ray photoelectron spectroscopy (XPS) was applied using a Thermo system (ESCALAB 250XI) with Al-Ka radiation. UV—visible (UV—Vis) absorption spectra were recorded on a DU-8B UV—vis double-beam spectrophotometer. Surface photovoltage (SPV) plots were recorded on a surface photovoltage spectrometer (PL-SPS/IPCE1000). The PEC measurements were carried out using a three-electrode system comprised of as-prepared samples as the working electrode, an Ag/AgCl reference electrode and a Pt counter electrode in 0.2 M Na_2SO_4 aqueous solution. A xenon lamp with calibrated intensity of 100 mW/cm^2 (AG 1.5G) was utilized as the light source. The Ag/AgCl potential can be converted into the reversible hydrogen electrode (RHE) potential using the following equation (1) [25]:

$$E_{RHE} = E_{Ag/AgCl} + 0.0591pH + 0.1976V \quad (1)$$

Electrochemical Impedance Spectroscopy (EIS) spectra were collected with an AC voltage amplitude of 5 mV in the dark. Mott-Schottky (M − S) plots were obtained at a frequency of 1000 Hz in the dark.

3. Results and discussion

The XRD patterns of WO_3, WO_3@α-Fe_2O_3 and WO_3@α-Fe_2O_3/FeOOH are shown in Fig. 2 and Fig. S1 to investigate their crystalline structure phase. Apart from the diffraction peaks marked with the symbol of "•" corresponding to SnO_2 originated from the FTO substrate, the peaks collected from WO_3 in Fig. 2a can be well indexed as monoclinic WO_3 (JCPDS: 72-0677). It can be clearly observed from Fig. 2b that the peaks marked with the symbol of "*" at 33.15°and 35.61° correspond to the (104) and (110) planes of rhombohedral phase α-Fe_2O_3 (JCPDS 33-0664). Besides, the remarkably increased peak at 24.13° is well agreement with α-Fe_2O_3. Noteworthy, there is no new phase formation after

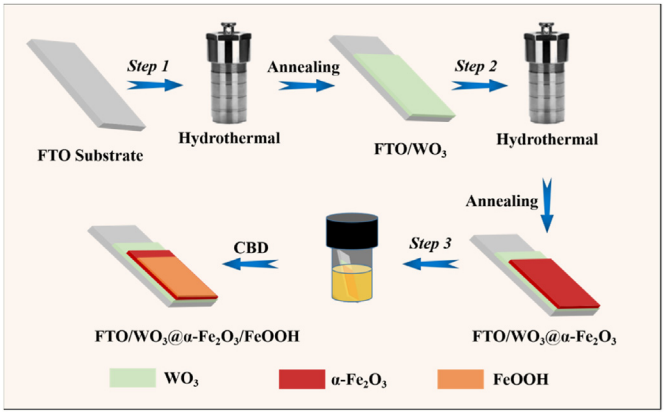

Fig. 1. Schematic illustration for the synthetic route of WO_3@α-Fe_2O_3/FeOOH composite.

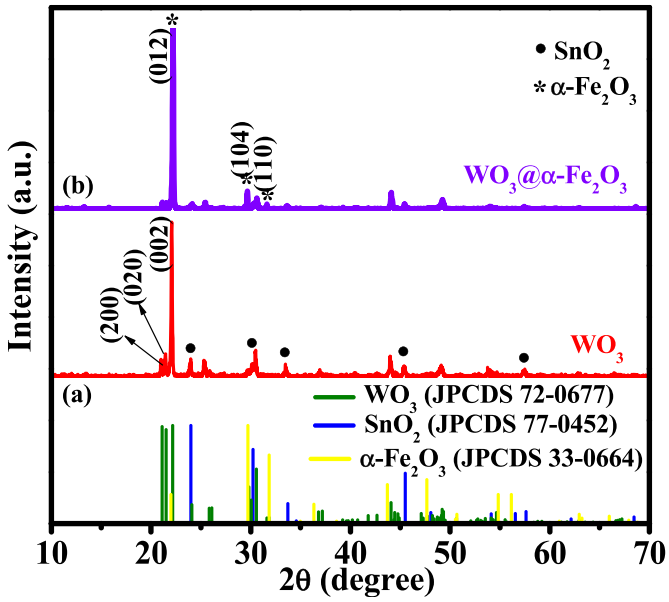

Fig. 2. XRD patterns of WO_3 and WO_3@α-Fe_2O_3 composite. Bottom lines are standard diffraction peaks of SnO_2, WO_3 and α-Fe_2O_3.

introduction of α-Fe_2O_3. These proof the successful fabrication of WO_3@α-Fe_2O_3. However, the diffraction peaks of FeOOH cannot be observed in Fig. S1 due to its amorphous phase [26].

SEM images of as-prepared samples are shown in Fig. 3 to characterize their surface morphologies. The WO_3 exhibits typically vertical smooth-faced nanorods (NRs) morphology with an average diameter of 200–300 nm and height of 2.56 μm approximately (Fig. 3a). As shown in Fig. 3b, the rice-like α-Fe_2O_3 with average length of 300–400 nm and diameters of about 50–100 nm decorate uniformly on the surface of WO_3 NRs, suggesting the successful formation of 3D core-shell WO_3@α-Fe_2O_3 structure. After depositing FeOOH layer, the surface morphology keeps almost unchanged, illustrating that the subsequent CBD process has no effect on its morphology. In order to further reveal the microstructures of WO_3@α-Fe_2O_3/FeOOH, the TEM and HRTEM imagines are obtained in Fig. 4 and Fig. S2. The lattice fringes with spacing of 0.369 nm and 0.269 nm can be assigned to the (200) plane of WO_3 and (104) plane of α-Fe_2O_3, respectively. The amorphous FeOOH layer with the thickness of approximately 2 nm is observed in Fig. S2, and it is highly uniform. Moreover, the EDS elemental mapping images (Fig. 4e) and corresponding elemental analysis spectrum (Fig. 4f) indicate the even distribution of W, O and Fe elements in WO_3@α-Fe_2O_3/FeOOH.

Specifically, the XPS measurement was conducted to investigate the surface compositions and valence states in WO_3@α-Fe_2O_3/FeOOH, and the high-resolution spectra of individual elements were obtained in Fig. 5. In Fig. 5a, three peaks located at 284.8 eV, 286.3 eV and 288.5 eV correspond to sp2 bonded carbon (C–C), carbonyls (C=O) and carboxyl (O=C–O) functional groups, respectively [27]. The high resolution in W 4f spectra (Fig. 5b) displays two peaks at 37.7 eV and 35.6 eV corresponding to $4f_{5/2}$ and $4f_{7/2}$ of W^{6+} [28]. The XPS spectrum of Fe 2p in Fig. 5c exhibits a peak at 710.7 eV for Fe $2p_{3/2}$, 724.6 eV for Fe $2p_{1/2}$, and a satellite peak, which are precisely assigned to the binding energies of Fe^{3+} in α-Fe_2O_3 phase [29]. In Fig. 5d, the O1s peaks at 529.9 eV and 531.4 eV can be attributed to the lattice oxygen (O^{2-}) and surface-absorbed O species (-OH) [30]. These results along with the XRD patterns and HRTEM imagines demonstrate the formation of WO_3@α-Fe_2O_3/FeOOH composite.

Subsequently, the UV–Vis spectras of all samples are obtained to illustrate their optical properties, and the optical band gap (E_g) can be calculated by the following equation (2) [31]:

$$(\alpha h\nu)^n = A(h\nu - Eg) \quad (2)$$

where α, h, ν and A are the absorbance coefficient, the Planck's constant, the vibration frequency and a constant, respectively. Besides, n is the vibration frequency of WO_3 (n = 2) due to its direct

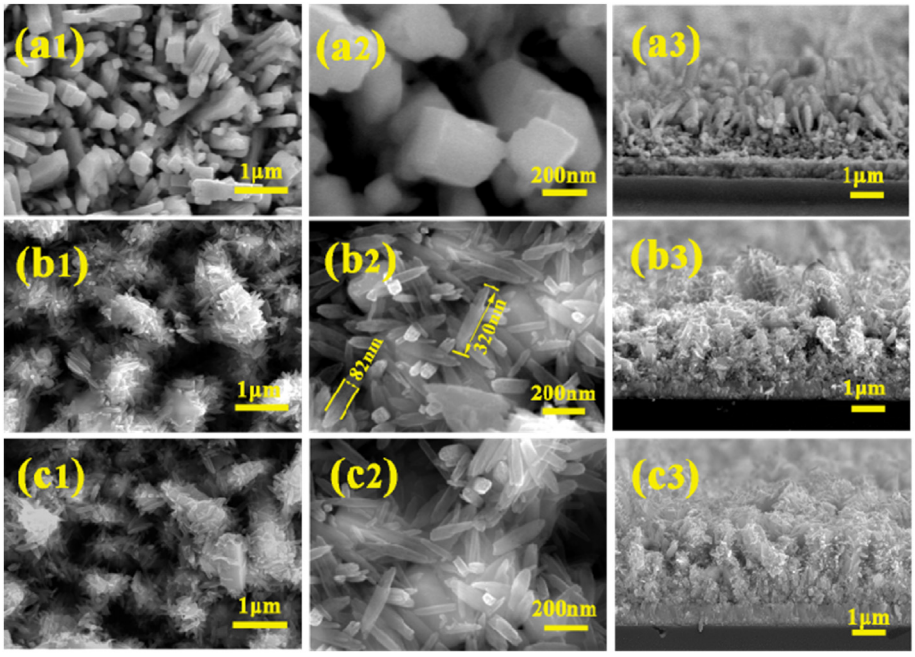

Fig. 3. (a1-a2) Top and (a3) cross-sectional view images of WO_3. (b1-b2) top and (b3) cross-sectional view images of WO_3@α-Fe_2O_3. (c1-c2) top and (c3) cross-sectional view images of WO_3@α-Fe_2O_3/FeOOH

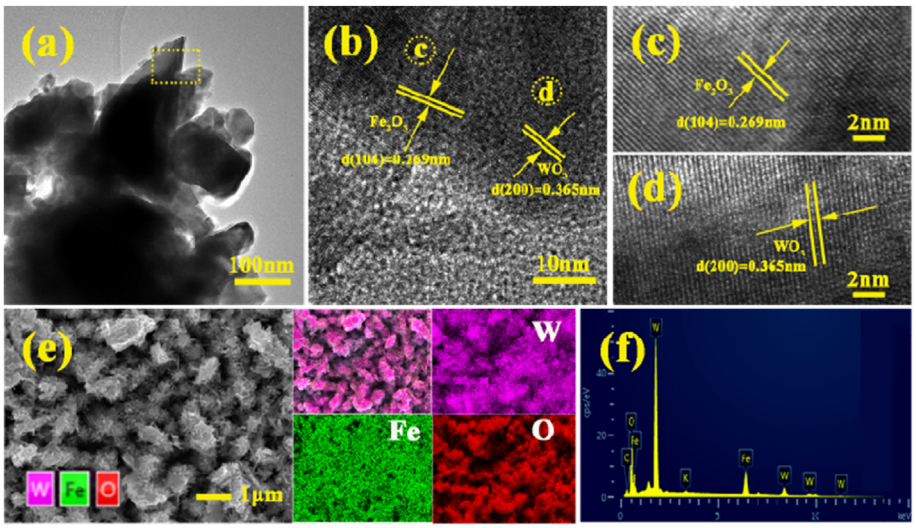

Fig. 4. (a) TEM image of WO_3@α-Fe_2O_3/FeOOH. (b) HRTEM image of the areas selected in (a). HRTEM images: (c) α-Fe_2O_3 and (d) WO_3. (e, f) EDS elemental analysis spectrum and corresponding elemental mapping images of W, O, and Fe, respectively.

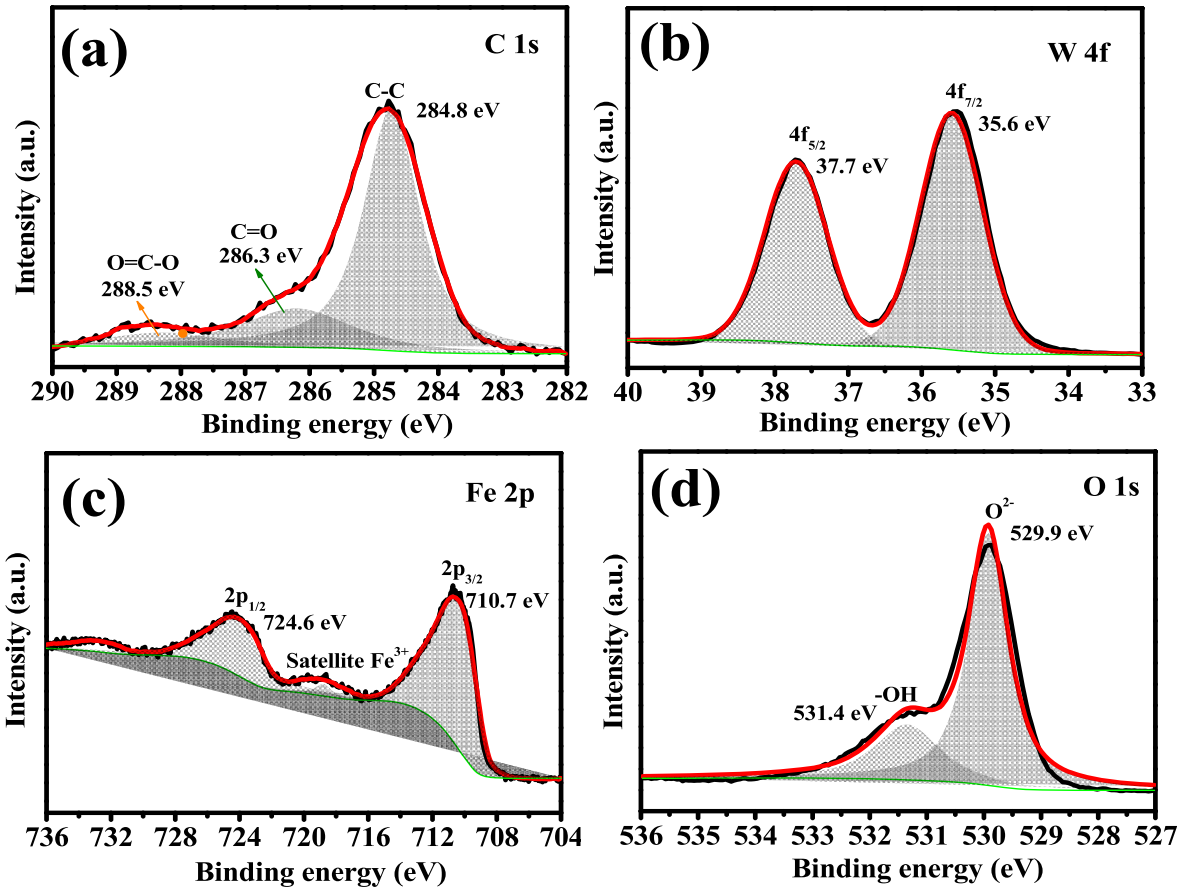

Fig. 5. High-resolution XPS: (a) C 1s, (b) W 4f, (c) Fe 2p and (d) O 1s.

band gap. From Fig. 6, it can be seen that the absorption edge of WO_3 locates at about 460 nm, corresponding to a band gap of 2.75 eV. Compared with WO_3, the WO_3@α-Fe_2O_3 shows a red-shift absorption range and increased visible light harvesting capability. It is worth noting that the bandgap of WO_3@α-Fe_2O_3 (2.16 eV) is very close to that of reported individual α-Fe_2O_3 (2.1 eV) [32,33], suggesting that α-Fe_2O_3 works as primary light absorber in 3D WO_3@α-Fe_2O_3 composite. After the deposition of ultrathin FeOOH layer, the absorption edge of WO_3@α-Fe_2O_3/FeOOH hardly changes.

As shown in Fig. 7a, the WO_3@α-Fe_2O_3 exhibits an enhanced photocurrent density of 0.65 mA/cm^2 at 1.23 V vs. RHE compared with WO_3 (0.30 mA/cm^2). The WO_3@α-Fe_2O_3/FeOOH yields the

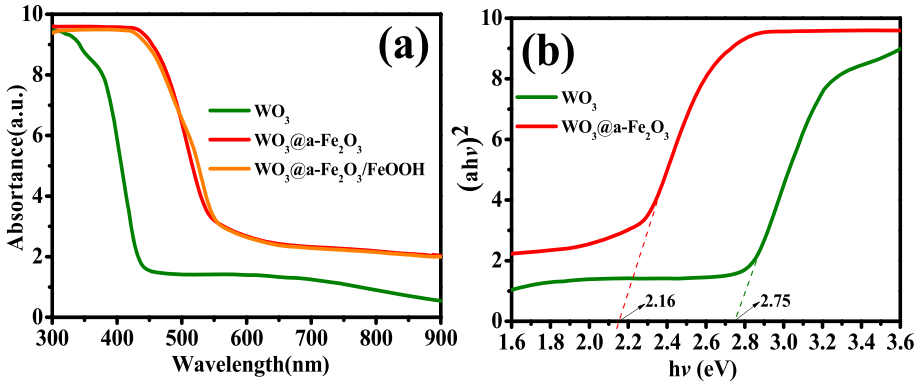

Fig. 6. (a) UV–Vis absorption spectrum of WO_3, WO_3@α-Fe_2O_3, and WO_3@α-Fe_2O_3/FeOOH. (b) Corresponding Tauc plots of WO_3 and WO_3@α-Fe_2O_3

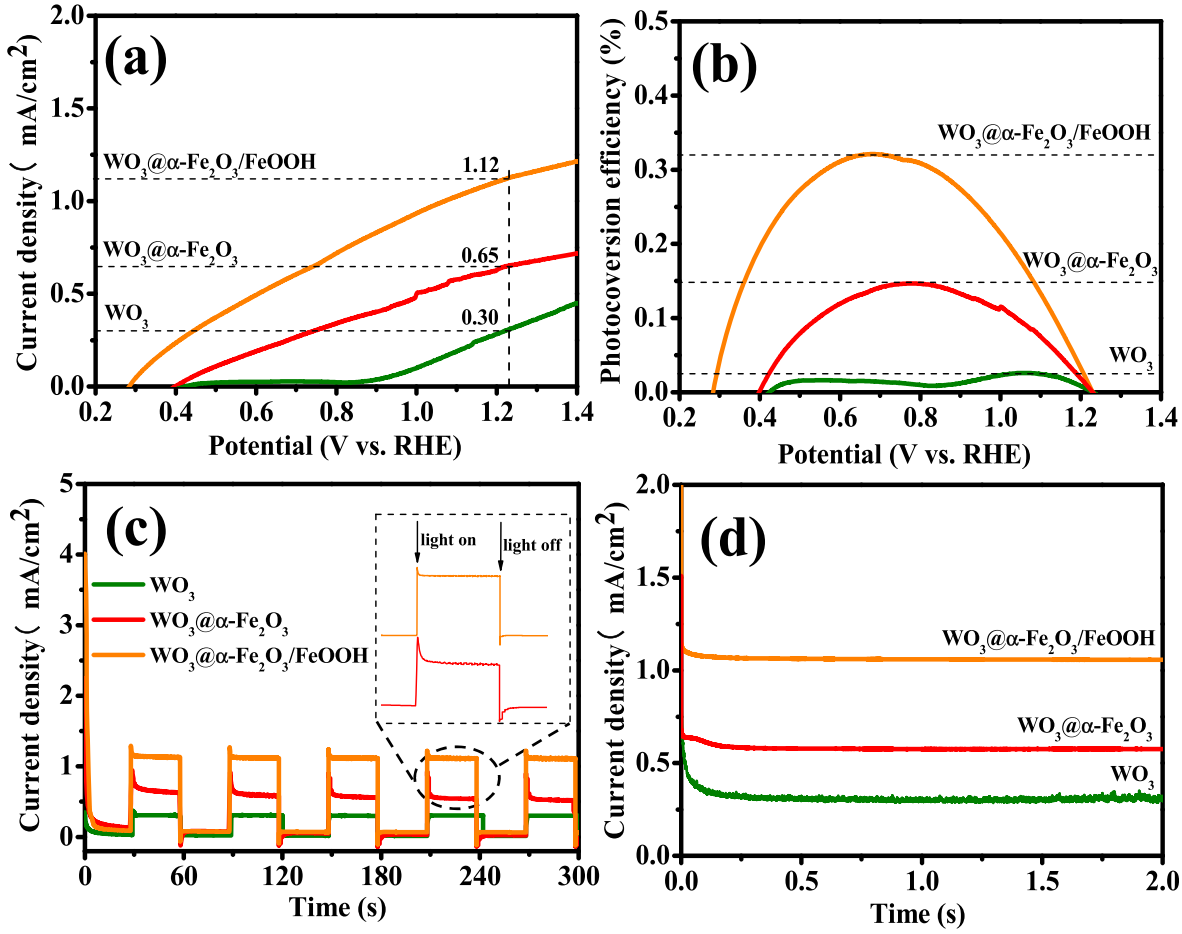

Fig. 7. (a) LSV plots of WO_3, WO_3@α-Fe_2O_3, and WO_3@α-Fe_2O_3/FeOOH photoanodes measured in 0.2 M Na_2SO_4 solution under AM 1.5 G illumination. (b) Calculated applied bias photon-to-current efficiency (ABPE) curves. (c) Transient photocurrent density versus time (I–T) curves. (d) Time-dependent photocurrent density curves measured at 1.23 V vs RHE under illumination.

highest photocurrent density value of 1.12 mA/cm^2 at 1.23 V vs. RHE. Besides, the photoanode exhibits a 120 mV negatively shifts in onset potential. Accordingly, the applied bias photon-to-current efficiency (ABPE) is calculated by equation (3) [33]:

$$\eta(\%) = J(1.23 - V) / P \times 100\% \quad (3)$$

where J is the measured photocurrent density (mA/cm^2), V is the applied bias (RHE) and P is the incident irradiance (100 mA/cm^2). As expected, the WO_3@α-Fe_2O_3/FeOOH achieves a maximum of 0.32% at a potential of 0.65 V vs. RHE (Fig. 7b). Moreover, the transient photocurrent density versus time (I-T) curves of all photoanodes are measured at 1.23 V vs RHE. As shown in Fig. 7c, the photocurrents of all the photoanodes quickly rise up and drop down once the light turns on and off, demonstrating their excellent transient photoresponse. Particularly, the sharp "spike" of WO_3@α-Fe_2O_3 can be observed in Fig. 7c which represent the accumulation of carriers at the moment of switching on and off the light,

indicating the slow water evolution oxygen dynamics of α-Fe_2O_3 [34]. After depositing ultrathin FeOOH layer, the "spike" of WO_3@α-Fe_2O_3/FeOOH is smaller, suggesting the improved water evolution oxygen dynamics and charge transport properties. Furthermore, the stability tests of all photoanodes were measured at 1.23 V vs RHE under AM 1.5G illumination. In Fig. 7d, no obvious decays of photocurrent density were observed during the rest, suggesting their excellent stability.

Afterwards, in order to investigate the effect of the WO_3@α-Fe_2O_3 on increased photocurrent, the SPV measurement was firstly carried out. To the best of our knowledge, SPV technology is used to characterize the surface density of photogenerated charges in the interface between WO_3 and α-Fe_2O_3, in other words, the stronger SPV signal means higher charge separation and transfer efficient [35]. In Fig. 8a, the WO_3 exhibits a weak positive SPV signal, which indicates the low separation efficiency of the photogenerated charges in WO_3. The significantly increased SPV signal can be observed after introduction of α-Fe_2O_3, which indicates that more photo-excited holes migrate to the irradiation side after separation, confirming that the WO_3@α-Fe_2O_3 heterojunction could promote photo-excited electron-hole pairs separation and transfer. Based on the above results along with the reported band energy position of WO_3 and α-Fe_2O_3, the charge separation and transfer process in WO_3@α-Fe_2O_3 heterojunction are shown in Fig. 8b. The conduction band position and valence band position of WO_3 are more positive than those of α-Fe_2O_3, which are favorable for the formation of

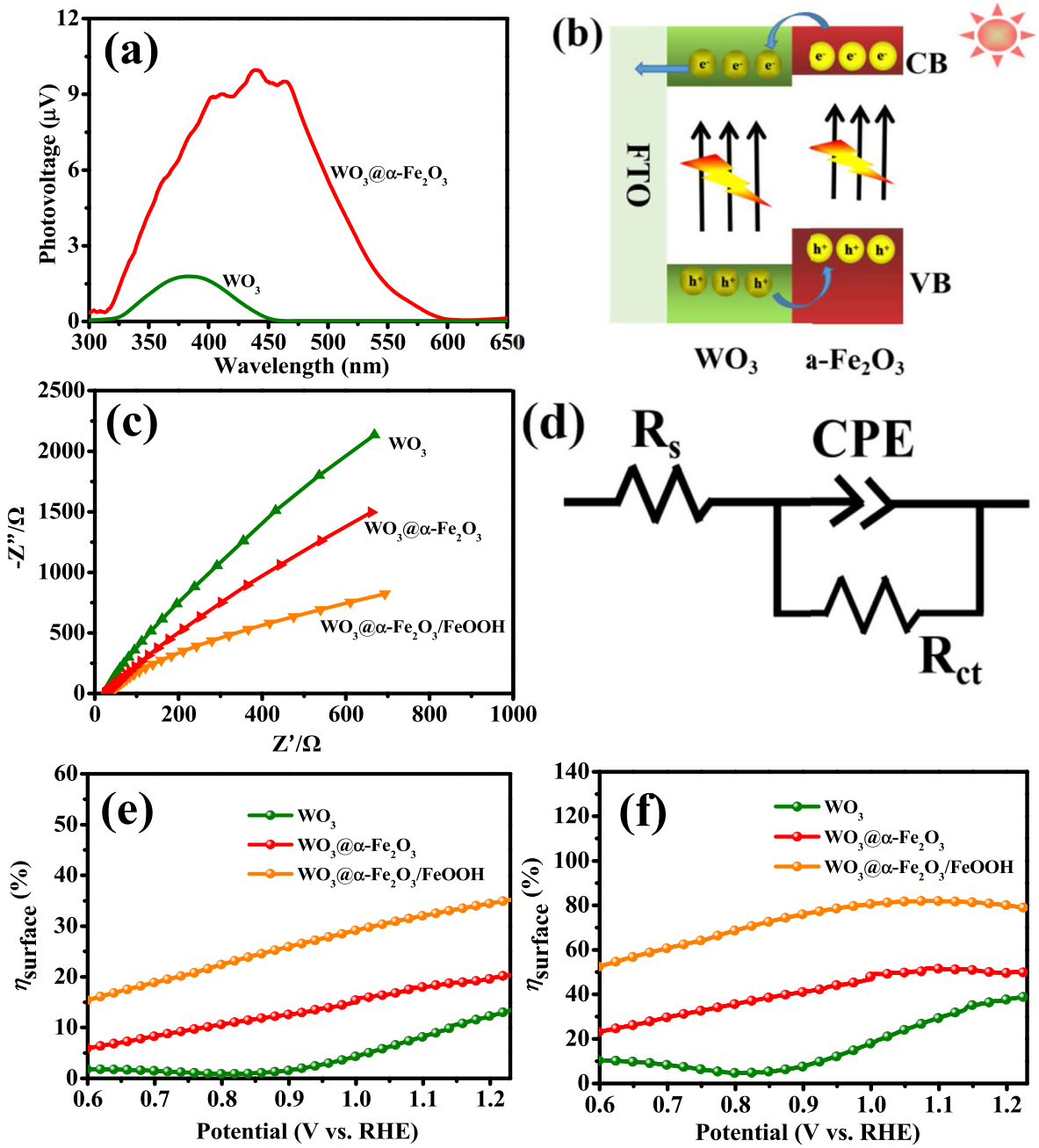

Fig. 8. (a) SPV spectroscopy of the photoanodes with front illumination. (b) Schematic diagram of the charge separation and transfer process in WO_3@α-Fe_2O_3 heterojunction. (c) EIS plots (d) the corresponding equivalent circuit. Charge separation efficiency (e) in the bulk (η_{bulk}) and (f) on the surface ($\eta_{surface}$).

type-II heterojunction structure. Under solar light excitation, the electron-hole pairs will be photoexcited both in WO_3 and Fe_2O_3. Therefore, the photogenerated electrons can easily transfer from the conduction band (CB) of Fe_2O_3 to the CB of WO_3, whereas the photogenerated holes of WO_3 are tend to injected to the valence band (VB) of α-Fe_2O_3. Hence, the WO_3@α-Fe_2O_3 heterojunction can facilitate the charge separation and transfer. It is noteworthy that the 1D WO_3 nanorods exhibit superior charge transport properties because they can offer the direct electron transport pathways with reduced grain boundaries, which further boost the charge separation and transfer [36]. Therefore, the 3D WO_3@α-Fe_2O_3 heterojunction structure shows an enhanced photocurrent density compared with WO_3 (Fig. 7a).

Hereafter, in order to conduct the role of ultrathin FeOOH layer, the EIS plots were obtained in Fig. 8c to elucidate the charger transfer resistance at the interface of electrode/electrolyte. Besides, an equivalent circuit model in Fig. 8d is adopted to fit the EIS data, in which R_s, R_{ct} and CPE are the electrolyte resistance, the charge transfer resistance at the photoelectrode/electrolyte interface and the constant phase element, respectively, and the consponding parameters are shown in Table S1. As shown in Fig. 8c, the lower charge transfer resistance can be observed in WO_3@α-Fe_2O_3 compared with WO_3 due to the heterojunction between WO_3 and α-Fe_2O_3, which can reduce the electron-hole recombination rate and accelerate the charge transfer. The WO_3@α-Fe_2O_3/FeOOH shows the smallest R_{ct} value, illustrating that charge can across photoelectrode/electrolyte interface more easily after depositing of ultrathin FeOOH layer, which can be attributed that the FeOOH acts as a hole transfer can promote the photogenerated holes shift to the electrode/electrolyte interface, avoiding the accumulation of photogenerated holes, thus, boosting the PEC performances.

To further quantify the effect of FeOOH layer, the charge separation efficiency in the bulk (η_{bulk}) and on the surface ($\eta_{surface}$) were determined by adding 0.1 M Na_2SO_3 hole scavenger into 0.2 M Na_2SO_3 electrolyte solution basced on equation (4) [12]:

$$J_{H_2O} = J_{abs} \times \eta_{\text{bulk}} \times \eta_{\text{surface}} \tag{4}$$

where J_{H2O} is the measured photocurrent density (Fig. 7a) and J_{Na2SO3} is the photocurrent density measured in the 0.2 M Na_2SO_4 electrolyte solution via adding 0.1 M Na_2SO_3 hole scavenger (Fig. S3). Notably, the charge separation efficiency on the surface is estimated to be 100% withe the presence of Na_2SO_3 as a hole scavenger. Thus, the η_{bulk} and $\eta_{surface}$ can be expressed as equations (5) and (6) [17,37]:

$$\eta_{\text{bulk}} = J_{Na_2SO_3} / J_{abs} \tag{5}$$

$$\eta_{\text{surface}} = J_{H_2O} / J_{Na_2SO_3} \tag{6}$$

In Fig. 8e, the η_{bulk} values of WO_3@α-Fe_2O_3 photoanode are much higher than those of WO_3 over the entire potential range, which could be attributed that the built-in electric field in the WO_3@α-Fe_2O_3 heterojunction improves the charge separation efficiency. It can be seen that the η_{sep} value of WO_3@α-Fe_2O_3/FeOOH photoanode reaches 35.57% at 1.23 V vs. RHE, which is almost 1.75 times than that of WO_3@α-Fe_2O_3 (20.31% at 1.23 V vs. RHE). Besides, the $\eta_{surface}$ value of WO_3@α-Fe_2O_3/FeOOH is 78.77% at 1.23 V vs. RHE, which is about 1.57 and 2.02 times than that of WO_3@α-Fe_2O_3 and WO_3, respectively. The great enhancement can be attribute to the ultrathin FeOOH layer acts as the hole transfer could accelerate the migration of holes to the photoelectrode/electrolyte interface to participate in the water oxidation reaction, decreasing the carrier recombination, thus, resulting in the improved photocurrent generation and onset potential shift for WO_3@α-Fe_2O_3/FeOOH photoanode in Fig. 7a.

In order to determine the carrier concentration (N_d) of all photoanodes, the M − S plots are obtained in Fig. 9. The N_d value can be calculated based on the following equations (7) and (8) [38]:

$$\frac{1}{C^2} = \left(\frac{2}{e\varepsilon\varepsilon_0 N_d A^2}\right)\left(V_A - V_{FB} - \frac{kT}{e}\right) \tag{7}$$

$$N_d = \frac{2}{e\varepsilon\varepsilon_0 A^2}\left[\frac{d\left(1/C^2\right)}{dV}\right]^{-1} \tag{8}$$

where C, V_A, V_{FB} and A are the space charge capacitance of semiconductor ($F \cdot cm^{-2}$), the applied potential (V), the flat band potential (V) and the photoactive area, respectively. e is elementary charge ($e = 1.602 \times 10^{-19}$ C), ε is the relative permittivity of WO_3, ε_0 is the permittivity of the vacuum ($\varepsilon_0 = 8.834 \times 10^{-12}$ F/m), and k is Boltzmanns constant ($k = 1.38 \times 10^{-23}$ F/m). As shown in Fig. 9, all the photoanodes show positive slopes corresponding to their n-type semiconductor characteristics. It can be seen that the WO_3@α-Fe_2O_3/FeOOH photoanode shows much higher carrier concentration than that of WO_3@α-Fe_2O_3, which is in line with the photocurrent values in Fig. 7a. This demonstrate that the ultrathin FeOOH layer as a hole transfer rapidly extract the holes at the surface of photoanode, which accelerates the water oxidation kinetics and further promotes the photogenerated electron-hole pairs separation and transfer.

On the basis of the above context, the mechanism of charge separation and transfer in WO_3@α-Fe_2O_3/FeOOH photoanode is proposed in Fig. 10. Under visible light irradiation, the photogenerated electrons in the conduction band of α-Fe_2O_3 can easily transfer to WO_3 [39], at the same time, the photo-generated holes in the valence band of WO_3 inject into that of α-Fe_2O_3 [40], driven by the internal electric field in WO_3@α-Fe_2O_3 heterojunction. Moreover, the WO_3@α-Fe_2O_3 heterojunction exerts respective advantages of 1D WO_3 (excellent electron transport pathways) and α-Fe_2O_3 (strong visible light absorption). Thus, an efficient spatial separation and transfer of electrons-hole pairs can be realized, which can be proved by SPV plots in Fig. 8a. After the deposition of ultrathin FeOOH hole transfer layer, the holes would further

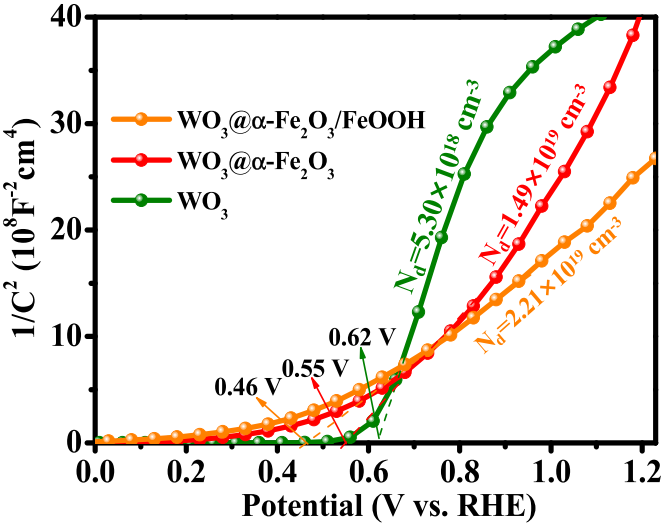

Fig. 9. Mott-Schottky (M − S) plots of WO_3, WO_3@α-Fe_2O_3, and WO_3@α-Fe_2O_3/FeOOH photoanodes measured at a frequency of 1 kHz in dark.

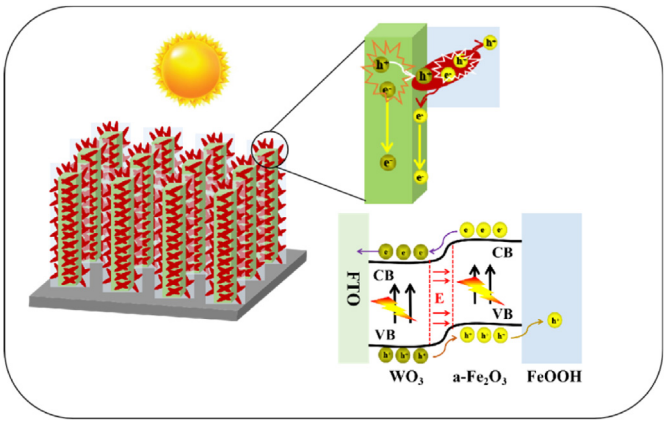

Fig. 10. Mechanism of charge separation and transfer in WO_3@α-Fe_2O_3/FeOOH photoanode.

transfer to FeOOH to the electrode/electrolyte interface quickly, which avoids the accumulation of photogenerated holes at the surface and reduces the charge-transfer barrier (Fig. 8c), leading to the great promoted separation efficiency on the surface in Fig. 8d. Consequently, the WO_3@α-Fe_2O_3/FeOOH photoanode yields significantly enhanced PEC performances under visible light.

4. Conclusion

In this work, a 3D core-shell WO_3@α-Fe_2O_3 photoanode modified by ultrathin FeOOH layer was designed and fabricated for efficient PEC performances. The α-Fe_2O_3 nanorices were firstly decorated on the surface of 1D WO_3 nanorods to form 3D core-shell WO_3@α-Fe_2O_3 heterojunction through a hydrothermal method and annealing treatment, then the ultrathin FeOOH layer was deposited via a facile chemical bath deposition (CBD) method. As expected, the WO_3@α-Fe_2O_3/FeOOH photoanode exhibits a 120 mV negatively shifts in onset potential and yields a photocurrent density of 1.12 mA/cm^2 at 1.23 V vs. RHE, which is 1.72 and 3.73 times than that of WO_3@α-Fe_2O_3 and WO_3 photoanodes, respectively. The great enhancement can be attributed to the WO_3@α-Fe_2O_3/FeOOH composite, which can exert respective advantages of 1D WO_3 (excellent electron transport pathways), α-Fe_2O_3 (strong visible light absorption) and FeOOH (a hole transfer) to boost visible light capture capability as well as the carrier separation and transfer efficiency in the bulk and on the surface, thus, leading to the significantly improved PEC performances.

Declaration of competing interest

The authors declare that they have no known competing financial interests or personal relationships that could have appeared to influence the work reported in this paper.

CRediT authorship contribution statement

Jin Zhang: Data curation, Writing - original draft, Writing - review & editing. **Gangqiang Zhu:** Conceptualization, Methodology. **Weiguo Liu:** Resources. **Yingxue Xi:** Project administration. **D.A. Golosov:** Formal analysis. **S.M. Zavadski:** Investigation. **S.N. Melnikov:** Validation.

Acknowledgements

This work was supported by the International Science and Technology Innovation Cooperation between Governments Project of National Key Research and Development Program (2018YFE0199200); Science and technology exchange programs between the governments of China and Belarus (CB02-19); National R&D Program of China (2017YFA0207400); Natural Science Basic Research Plan in Shaanxi Province of China (2017JM5022); Open Fund of Shaanxi Province Key Laboratory of Thin Films Technology and Optical Test (ZSKJ201706) and Xi'an Key Laboratory of Intelligent Detection and Perception (201805061ZD12CG45).

Appendix A. Supplementary data

Supplementary data to this article can be found online at https://doi.org/10.1016/j.jallcom.2020.154992.

References

[1] A. Fujishima, K. Honda, Electrochemical photolysis of water at a semiconductor electrode, Nature 238 (1972) 37–38.
[2] H.D. She, P.F. Yue, X.Y. Ma, J.W. Huang, L. Wang, Q.Z. Wang, Fabrication of $BiVO_4$ photoanode cocatalyzed with NiCo-layered double hydroxide for enhanced photoactivity of water oxidation, Appl. Catal. B Environ. 263 (2020) 118280.
[3] W. Wang, M.G. Xu, X.M. Xu, W. Zhou, Z.P. Shao, Perovskite oxide based electrodes for high-performance photoelectrochemical water splitting, Angew. Chem. Int. Ed. 59 (2020) 136–152.
[4] X.F. Long, F. Li, L.L. Gao, Y.P. Hu, H.G. Hu, J. Jin, J.T. Ma, Heterojunction and oxygen vacancy modification of ZnO nanorod array photoanode for enhanced photoelectrochemical water splitting, ChemSusChem 11 (2018) 4094–4101.
[5] J.C. Liu, S.M. Xu, Y.F. Li, R.K. Zhang, M.F. Shao, Facet engineering of WO_3 arrays toward highly efficient and stable photoelectrochemical hydrogen generation from natural seawater, Appl. Catal. B Environ. 264 (2020) 118540.
[6] Z.F. Liu, J.Y. Wu, J. Zhang, Quantum dots and plasmonic Ag decorated WO_3 nanorod photoanodes with enhanced photoelectrochemical performances, Int. J. Hydrogen Energy 42 (2016) 20529–20535.
[7] D. Chen, Z.F. Liu, S.C. Zhang, Enhanced PEC performance of hematite photoanode coupled with bimetallic oxyhydroxide NiFeOOH through a simple electroless method, Appl. Catal., B 265 (2020) 118580.
[8] D. Chen, Z.F. Liu, M. Zhou, P.D. Wu, J.D. Wei, Enhanced photoelectrochemical water splitting performance of α-Fe_2O_3 nanostructures modified with Sb_2S_3 and cobalt phosphate, J. Alloys Compd. 742 (2018) 918–927.
[9] J.H. Sun, L.X. Sun, X.J. Yang, S.L. Bai, R.X. Luo, D.Q. Li, A.F. Chen, Photoanode of coupling semiconductor heterojunction and catalyst for solar PEC water splitting, Electrochim. Acta 331 (2020) 135282.
[10] Y.D. Wang, W. Tian, C. Chen, W.W. Xu, L. Li, Tungsten trioxide nanostructures for photoelectrochemical water splitting: material engineering and charge carrier dynamic manipulation, Adv. Funct. Mater. 29 (2019) 1809036.
[11] G.W. Zheng, J.S. Wang, H. Liu, V. Murugadoss, G.N. Zu, H.B. Che, C. Lai, H.Y. Li, T. Ding, Q. Gao, Z.H. Guo, Tungsten oxide nanostructures and nanocomposites for photoelectrochemical water splitting, Nanoscale 11 (2019) 18968–18994.
[12] Y.T. Li, Z.F. Liu, M.N. Ruan, Z.G. Guo, X.F. Li, The 1D WO_3nanorods/2D WO_{3-x} nanoflakes homojunction structure for enhanced charge separation and transfer towards efficient photoelectrochemical performance, ChemSusChem 12 (2019) 5282–5290.
[13] J. Zhang, Z.H. Liu, Z.F. Liu, Novel WO_3/Sb_2S_3 heterojunction photocatalyst based on WO_3 of different morphologies for enhanced efficiency in photoelectrochemical water splitting, ACS Appl. Mater. Interfaces 8 (2016) 9684–9691.
[14] C.J. Liu, Y.H. Yang, J. Li, S. Chen, W.Z. Li, X.D. Tang, An in situ transformation approach for fabrication of $BiVO_4/WO_3$ heterojunction photoanode with high photoelectrochemical activity, Chem. Eng. J. 326 (2017) 603–611.
[15] G.M. Carroll, D.R. Gamelin, Kinetic analysis of photoelectrochemical water oxidation by mesostructured Co-Pi/α-Fe_2O_3 photoanodes, J. Mater. Chem. A. 4 (2016) 2986–2994.
[16] D. Chen, Z.F. Liu, Z.G. Guo, W.G. Yan, Y. Xin, Enhancing light harvesting and charge separation of Cu_2O photocathodes with spatially separated noble-metal cocatalysts towards highly efficient water splitting, J. Mater. Chem. A. 6 (2018) 20393–20401.
[17] D. Chen, Z.F. Liu, Z.G. Guo, M.N. Ruan, W.G. Yan, 3D branched Ca-Fe_2O_3/Fe_2O_3 decorated with Pt and Co-Pi: improved charge separation dynamics and photoelectrochemical performance, ChemSusChem 12 (2019) 3286–3295.
[18] F. Malara, A. Minguzzi, M. Marelli, S. Morandi, R. Psaro, V.D. Santo, A. Naldoni, α-Fe_2O_3/NiOOH: an effective heterostructure for photoelectrochemical water oxidation, ACS Catal. 5 (2015) 5292–5300.
[19] A.G. Tamirat, A.A. Dubale, W.N. Su, H.M. Chen, B.J. Hwang, Sequentially surface modified hematite enables lower applied bias photoelectrochemical water splitting, Phys. Chem. Chem. Phys. 19 (2017) 20881–20890.
[20] J. Lee, H. Lee, B. Lim, Chemical transformation of iron alkoxide nanosheets to FeOOH nanoparticles for highly active and stable oxygen evolution electrocatalysts, J. Ind. Eng. Chem. 58 (2018) 100–104.

[21] M. Zhou, Z.H. Liu, X.F. Li, Z.F. Liu, Promising three-dimensional flowerlike $CuWO_4$ photoanode modified with CdS and FeOOH for efficient photoelectrochemical water splitting, Ind. Eng. Chem. Res. 57 (2018) 6210–6217.
[22] B.B. Zhang, L. Wang, Y.J. Zhang, Y. Ding, Y.P. Bi, Ultrathin FeOOH nanolayers with abundant oxygen vacancies on $BiVO_4$ photoanodes for efficient water oxidation, Angew. Chem. Int. Ed. 57 (2018) 2248–2252.
[23] S.L. Kuang, M. Wang, Z.B. Geng, X.F. Wu, Y. Sun, W. Ma, D.S. Chen, J.H. Liu, S.H. Feng, K.K. Huang, Enhancement of Fe_2TiO_5 photoanode through surface Al^{3+} treatment and FeOOH modification, ACS Sustain. Chem. Eng. 7 (2019) 14347–14352.
[24] Y.T. Li, Z.F. Liu, Z.G. Guo, M.N. Ruan, X.F. Li, Y.L. Liu, Efficient WO_3 photoanode modified by Pt layer and plasmonic Ag for enhanced charge separation and transfer to promote photoelectrochemical performances, ACS Sustain. Chem. Eng. 7 (2019) 12582–12590.
[25] Z.F. Liu, Q.G. Song, M. Zhou, Z.G. Guo, J.H. Kang, H.Y. Yan, Synergistic enhancement of charge management and surface reaction kinetics by spatially separated cocatalysts and p-n heterojunctions in $Pt/CuWO_4/Co_3O_4$ photoanode, Chem. Eng. J. 374 (2019) 554–563.
[26] L. Guo, K.L. Zhang, X.X. Han, Q. Zhao, D.J. Wang, F. Fu, Y.C. Liang, Highly efficient visible-light-driven photo-Fenton catalytic performance over FeOOH/Bi_2WO_6 composite for organic pollutant degradation, J. Alloys Compd. 816 (2020) 152560.
[27] G.Q. Zhu, S.P. Li, J.Z. Gao, F.C. Zhang, C.L. Liu, Q.Z. Wang, M. Hojamberdiev, Constructing a 2D/2D $Bi_2O_2CO_3/Bi_4O_5Br_2$ heterostructure as a direct Z-scheme photocatalyst with enhanced photocatalytic activity for NO_x removal, Appl. Surf. Sci. 493 (27) (2019) 913–925.
[28] F. Zheng, J. Wang, W.B. Liu, J.M. Zhou, H. Li, Y. Yu, P.F. Hu, W. Yan, Y. Liu, R. Li, Q. Zhen, J.J. Zhang, Novel diverse-structured h-WO_3 nanoflake arrays as electrode materials for high performance supercapacitors, Electrochim. Acta 334 (2020) 135641.
[29] G.M. Wang, Y.C. Ling, D.A. Wheeler, K.E.N. George, K. Horsley, C. Heske, J.Z. Zhang, Y. Li, Facile synthesis of highly photoactive α-Fe_2O_3-based films for water oxidation, Nano Lett. 11 (2011) 3503–3509.
[30] F. Rao, G.Q. Zhu, M. Hojamberdiev, W.B. Zhang, S.P. Li, J.Z. Gao, F.C. Zhang, Y.H. Huang, Y. Huang, Uniform Zn^{2+}-doped BiOI microspheres assembled by ultrathin nanosheets with tunable oxygen vacancies for super-stable removal of NO, J. Phys. Chem. C 123 (2019) 16268–16280.
[31] W.Z. Li, L.B. Du, Q. Liu, Y. Liu, D.W. Li, J. Li, Trimetallic oxyhydroxide modified 3D coral-like $BiVO_4$ photoanode for efficient solar water splitting, Chem. Eng. J. 384 (2020) 123323.
[32] Z.W. Fu, T.F. Jiang, Z.P. Liu, D.J. Wang, L.L. Wang, T.F. Xie, Highly photoactive Ti-doped α-Fe_2O_3 nanorod arrays photoanode prepared by a hydrothermal method for photoelectrochemical water splitting, Electrochim. Acta 129 (2014) 358–363.
[33] T.T. Yang, J.W. Xue, H. Tan, A.J. Xie, S.K. Li, W.S. Yan, Y.H. Shen, Highly ordered ZnO/$ZnFe_2O_4$ inverse opals with binder-free heterojunction interfaces for high-performance photoelectrochemical water splitting, J. Mater. Chem. A. 6 (2018) 1210–1218.
[34] D. Chen, Z. Liu, Dual-axial gradient doping (Zr and Sn) on hematite for promoting charge separation in photoelectrochemical water splitting, ChemSusChem 11 (2018) 3438–3448.
[35] M.L. Kang, J.M. Liang, F.F. Wang, X.B. Chen, Y. Lu, J. Zhang, Structural design of hexagonal/monoclinic WO_3 phase junction for photocatalytic degradation, Mater. Res. Bull. 121 (2020) 110614.
[36] J.Z. Su, X.J. Feng, J.D. Sloppy, L.J. Guo, C.A. Grimes, Vertically aligned WO_3 nanowire arrays grown directly on transparent conducting oxide coated glass: synthesis and photoelectrochemical properties, Nano Lett. 11 (2011) 203–208.
[37] Y.T. Li, Z.F. Liu, J. Zhang, Z.G. Guo, Y. Xin, L. Zhao, 1D/0D WO_3/CdS heterojunction photoanodes modified with dual co-catalysts for efficient photoelectrochemical water splitting, J. Alloys Compd. 790 (2019) 493–501.
[38] J. Guo, X.J. Yang, S.L. Bai, X. Xiang, R.X. Luo, J. He, A.F. Chen, Effect of Mo doping and NiFe-LDH cocatalyst on PEC water oxidation efficiency, J. Colloid Interface Sci. 540 (2019) 9–19.
[39] R.B. Wei, P.Y. Kuang, H. Cheng, Y.B. Chen, J.Y. Long, M.Y. Zhang, Z.Q. Liu, Highly efficient and stable gold NPs decorated ZnO/CdS nanotube arrays photoanode for enhanced photoelectrochemical water splitting, ACS Sustain. Chem. Eng. 5 (2017) 4249–4257.
[40] B.F. Zheng, T. Ouyang, Z. Wang, J.Y. Long, Y.B. Chen, Z.Q. Liu, Enhanced plasmon-driven photoelectrocatalytic methanol oxidation on Au decorated α-Fe_2O_3 nanotube arrays, Chem. Commun. (J. Chem. Soc. Sect. D) 54 (2018) 9583–9586.